

Lab on a Chip

Accepted Manuscript



This is an *Accepted Manuscript*, which has been through the Royal Society of Chemistry peer review process and has been accepted for publication.

Accepted Manuscripts are published online shortly after acceptance, before technical editing, formatting and proof reading. Using this free service, authors can make their results available to the community, in citable form, before we publish the edited article. We will replace this *Accepted Manuscript* with the edited and formatted *Advance Article* as soon as it is available.

You can find more information about *Accepted Manuscripts* in the [Information for Authors](#).

Please note that technical editing may introduce minor changes to the text and/or graphics, which may alter content. The journal's standard [Terms & Conditions](#) and the [Ethical guidelines](#) still apply. In no event shall the Royal Society of Chemistry be held responsible for any errors or omissions in this *Accepted Manuscript* or any consequences arising from the use of any information it contains.

High Process Yield Rates of Thermoplastic Nanofluidic Devices using a Hybrid Thermal Assembly Technique

Franklin I. Uba,^{1‡} Bo Hu,^{3‡} Kumuditha Weerakoon-Ratnayake,⁴ Nyote Oliver-Calixte,⁴ and Steven A. Soper^{1,2,5*}

¹Department of Chemistry, UNC-Chapel Hill, NC, 27599

²Department of Biomedical Engineering, UNC-Chapel Hill, NCSU, Raleigh, NC

³Research Center for Analytical Sciences, Northeastern University, Box 332, Shenyang 110004, China

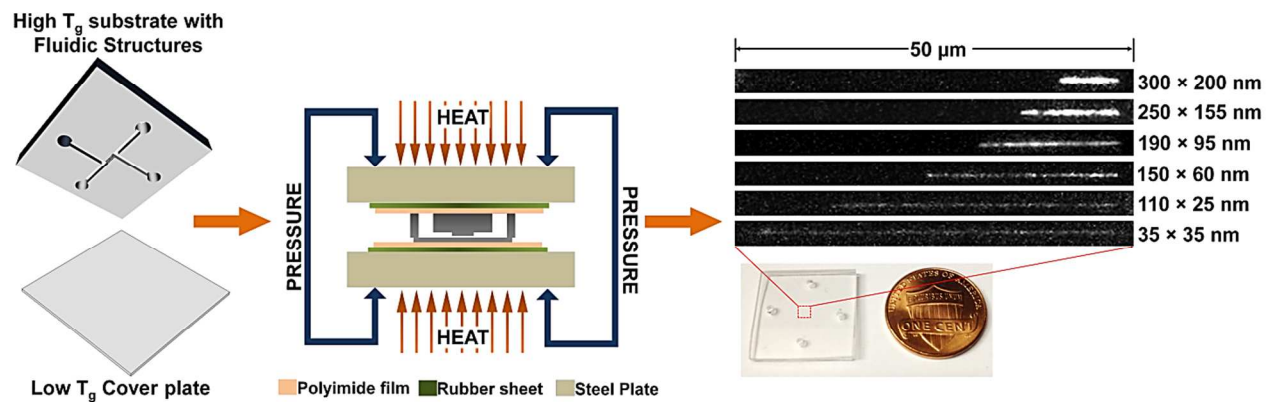
⁴Department of Chemistry, Louisiana State University, Baton-Rouge, LA, 70803

⁵Ulsan National Institute of Science and Technology, Ulsan, S. Korea

[‡]Authors contributed equally

*corresponding author ssoper@unc.edu

TABLE OF CONTENT GRAPHIC



A low temperature hybrid assembly process for the production of functional thermoplastic nanofluidic devices with process yield rates $>90\%$ and an assembly time of 16 min is reported.

ABSTRACT

Over the past decade, thermoplastics have been used as alternative substrates to glass and Si for microfluidic devices because of the diverse and robust fabrication protocols available for thermoplastics that can generate high production rates of the desired structures at low cost and with high replication fidelity, the extensive array of physiochemical properties they possess, and the simple surface activation strategies that can be employed to tune their surface chemistry appropriate for the intended application. While the advantages of polymer microfluidics are currently being realized, the evolution of thermoplastic-based nanofluidic devices is fraught with challenges. One challenge is assembly of the device, which consists of sealing a cover plate to the patterned fluidic substrate. Typically, channel collapse or substrate dissolution occurs during assembly making the device inoperable resulting in low process yield rates. In this work, we report a low temperature hybrid assembly approach for the generation of functional thermoplastic nanofluidic devices with high process yield rates (>90%) with a short total assembly time (16 min). The approach involves thermally sealing a high T_g (glass transition temperature) substrate containing the nanofluidic structures to a cover plate possessing a lower T_g . Nanofluidic devices with critical feature sizes ranging between 25 – 250 nm were fabricated in a thermoplastic substrate ($T_g = 104^\circ\text{C}$) and sealed with a cover plate ($T_g = 75^\circ\text{C}$) at a temperature significantly below the T_g of the substrate. Results obtained from sealing tests revealed that the integrity of the nanochannels remained intact after assembly and devices were useful for fluorescence imaging at high signal-to-noise ratios. The functionality of the assembled devices was demonstrated by studying the stretching and translocation dynamics of dsDNA in the enclosed thermoplastic nanofluidic channels.

Keywords: Nanofluidics, Thermoplastics, Thermal Fusion Bonding, DNA translocation

INTRODUCTION

Nanofluidic devices have generated great interest for investigating several unique physical and chemical phenomena that are not observable in micro-scale environments. For example, nanofluidic devices have served as viable platforms for the analysis of biopolymers, especially DNAs.^{1, 2} When a double-stranded DNA (dsDNA) molecule is contained in a microchannel, it will assume a randomly coiled-state (low entropy) with a radius of gyration (R_g) defined by the ionic strength of the solution and the contour length of the molecule.³ However, when confined in a nanochannel with dimensions (width \times depth) comparable to its persistence length, ~ 50 nm for dsDNA, the molecule stretches with the degree of stretching inversely proportional to the nanochannel dimensions.⁴⁻⁷ This phenomenon has generated interesting applications such as identification of methylation patterns within dsDNA,⁸ restriction mapping of genomic DNA,⁹ DNA fragment sizing,¹⁰ localization of transcription factors for protein synthesis,¹¹ and high signal-to-noise ratio detection of single DNA molecules.¹²

Recently, polymer-based materials, especially thermoplastics – linear or branched polymers – have become attractive substrates for the fabrication of fluidic devices. Thermoplastics, such as poly(methylmethacrylate), PMMA, polycarbonate, PC, cyclic olefin copolymer, COC, and polyethylene terephthalate, PET, possess glass transition temperatures (T_g) that are significantly lower than that of glass allowing for the fabrication of nanostructures using nanoimprint lithography (NIL), which is conducive to high production rates of devices at low cost and with good replication fidelity.¹³ NIL has been successful in patterning structures to the sub-10 nm scale with the ultimate resolution seemingly determined by the minimum feature size associated with the molding tool.¹⁴⁻¹⁷ Other techniques that can be used to fabricate thermoplastic nanostructures include proton beam writing,¹⁸ thermomechanical deformation,¹⁹ compression of microchannels,²⁰ sidewall lithography,²¹ UV-lithography/ O_2 plasma etching,²² hot embossing

with thermoplastic molding tools,²³ refill of microchannels,²⁴ and the use of silica nanowire templates.²⁵

The aforementioned techniques for producing nanostructures in thermoplastics employed a top-down approach and as such, an assembly step is required to enclose the fluidic network. Unfortunately, challenges associated with assembling devices with cover plates have limited the use of thermoplastic nanofluidic devices with the smallest operational thermoplastic nanochannel device reported to-date possessing dimensions of 71×77 nm (width \times depth).¹⁶ The limitation of using thermoplastic nanofluidic devices has arisen predominately from collapse of the cover plate into the fluidic channel and/or deformation of the thermoplastic nanochannels during assembly, generating low process yield rates, typically $<40\%$ (process yield rate = percentage of devices that possess dimensions comparable to design parameters and are functional).

In a typical fluidic device production pipeline, the final step involves fusion bonding the substrate possessing the fluidic network to a second material (cover plate) that encloses the channels. The common modes employed for enclosing thermoplastic nanochannels are thermal or solvent-assisted fusion bonding.²⁶ Thermal fusion bonding a substrate to a cover plate of the same material has been executed by: (i) Heating the substrate and cover plate to a temperature slightly above their T_g while applying a constant pressure allowing the polymer chains to diffuse between the contact surfaces; or (ii) bonding at a temperature lower than the T_g of the material by using UV/O₃ or oxygen plasma treatment of the substrate and cover plate prior to chip assembly, thereby reducing the T_g of the first few monolayers of material.^{15-17, 27, 28} Although both approaches have been reported to produce high tensile strength between the cover plate and substrate, the first approach is typically discouraged for assembly of thermoplastic nanofluidic devices because it results in bulk polymer flow and significant deformation or collapse of the

nanochannels (40% and 60% deformation for PMMA and COC, respectively) rendering devices unusable in most cases (*i.e.*, low process yield rates). The second approach is commonly used for enclosing thermoplastic nanochannels, however, the resulting bond strength is often lower than desired and thus, are unable to withstand high pressure or electric fields for extended periods of time.¹⁵ Preliminary results obtained from our group have revealed that nanochannels experience reduction in depths (6% for PMMA and 9% for COC) when sealed with cover plates of the same material by thermal fusion bonding at a temperature below its bulk T_g after O_2 plasma treatment.¹⁵ Unfortunately, these channel dimensional changes increase as the nanochannel dimensions drop below 50 nm and result in low process yield rates. Likewise, solvent-assisted bonding suffers from problems associated with dimensional stability because the solvent can soften the plastic material leading to material dissolution.²⁶ Hence, there remains the need for the development of methods for assembling thermoplastic nanochannels with high bond strengths while maintaining structural integrity and producing high process yield rates.

Herein, we report a robust method for the assembly of thermoplastic nanofluidic devices in which a high T_g thermoplastic substrate possessing the nanofluidic structures is bonded to a cover plate with a T_g lower than that of the substrate. Although, a similar scheme was reported for assembling COC-based microsystems²⁹ and recently for assembling PMMA nanochannels using a PET cover plate,³⁰ the smallest assembled nanochannels were ~ 85 nm and the functionality of these devices for biological applications were not demonstrated. In this study, COC ($T_g = 75^\circ\text{C}$) was used as the cover plate due to its excellent optical transmissivity (with low propagation loss at $\lambda > 300$ nm), low autofluorescence,^{31, 32} low moisture uptake ($< 0.01\%$), high temperature tolerance, chemical resistance and ease of surface modification via UV/ O_3 activation or O_2 plasma treatment. The T_g of COC depends on the norbornene content and can range from

65 – 180°C for norbornene contents ranging from 60 – 85 wt%, respectively.^{29, 33} Nanofluidic channels were fabricated in a substrate (PMMA; $T_g = 105^\circ\text{C}$ or COC; $T_g = 108^\circ\text{C}$) via a single imprinting step as previously reported.³⁴ Device assembly was achieved by bonding a plasma treated cover plate (COC; $T_g = 75^\circ\text{C}$) to an untreated substrate at a temperature $\sim 5^\circ\text{C}$ lower than the T_g of the cover plate. In contrast to the high temperature, time-consuming and long processing steps required for enclosing glass nanofluidic devices producing low process yield rates,^{35, 36} our assembly process was performed directly on the thermoplastic substrate following embossing without the need for pre-cleaning in RCA solutions or organic solvents in a total processing time of 16 min and process yield rates exceeding 90%. With this assembly approach, we demonstrate the use of sub-50 nm thermoplastic nanochannels for high SNR fluorescence imaging and DNA stretching. Finally, nanochannels were UV/O₃ activated through the cover plate post-assembly and the functionality of the assembled devices assessed by investigating the transport dynamics of dsDNA through the nanochannels as well as the surface charge.

EXPERIMENTAL METHODS

Materials and reagents. PMMA sheets ($T_g = 105^\circ\text{C}$), 1.5 mm and 0.175 mm thick, were purchased from Good Fellow (Berwyn, PA). COC 6017 ($T_g \approx 178^\circ\text{C}$), 5010 ($T_g \approx 108^\circ\text{C}$) and 8007 ($T_g \approx 78^\circ\text{C}$; 0.13 mm) sheets were purchased from TOPAS Advanced Polymers (Florence KY). Si <100> wafers were secured from University Wafers (Boston, MA). Tripropylene glycol diacrylate (TPGA), trimethylolpropane triacrylate (TMPA), Irgacure 651 (photo-initiator), 50% potassium hydroxide (KOH), hydrochloric acid (HCl) and potassium chloride (KCl) were obtained from Sigma-Aldrich (St. Louis, MO). The anti-adhesion monolayer of (tridecafluoro – 1,1,2,2 – tetrahydrooctyl) trichlorosilane (T-silane) was purchased from Gelest, Inc. Tris buffer

(pH = 8.0) was obtained from Fisher Scientific (Houston, TX). All dilutions were performed using 18 M Ω /cm milliQ water (Millipore).

Device fabrication. Nanofluidic structures were fabricated in thermoplastic substrates using a scheme previously reported by our group.³⁴ Briefly, access microchannels and nanochannels were fabricated in a Si wafer (master) by optical lithography and focused-ion beam milling, respectively. Next, resin stamps were produced from the Si master by curing a UV-resin (68 wt% TPGA, 28 wt% TMPA and 4 wt% Irgacure 651) under 365 nm light coated onto a COC plate ($T_g = 178^\circ\text{C}$). Subsequently, fluidic structures were imprinted into the polymer substrate by thermal embossing at 125°C for 120 s under 1910 kN/m^2 pressure using a Hex03 hot embosser (JenOptik). In the final fabrication step, fluidic structures were enclosed with a low T_g thermoplastic cover plate using the setup shown in Fig. 1a.

The assembly scheme (see Fig. 1b) used a substrate possessing the fluidic structures and an oxygen plasma treated cover plate that were brought into conformal contact and placed in a vacuum seal bag to eliminate air pockets from the contacted substrate/cover plate. Next, the partially bonded device (determined by the lack of Newton rings) was sandwiched between a pair of polyimide films, rubber sheets and placed between the platens of the thermal embosser (see Fig. 1a). We found that the rubber sheets promoted bond uniformity across the entire surfaces while the polyimide film prevented sticking of the thermoplastic nanofluidic device to the rubber sheets. The temperature, pressure and time were found to be important process parameters, which depended primarily on the thermal, mechanical, physical and surface properties of the cover plate. As shown in Fig. 1b, the temperature–pressure program used for enclosing the fluidic structures was partitioned into six stages:

- 1) Touch force stage – This was used to facilitate heat conduction across the surfaces prior to thermal fusion bonding. The top and bottom embosser platens were advanced towards the assembly and used to clamp the pre-assembled substrate/cover plate near room temperature at a pressure of 180 kN/m^2 , which was lower than the required assembly pressure.
- 2) Heating Stage – The top and bottom platens were heated to the optimized assembly temperature (70°C when using the COC 8007 cover plate) at a ramp rate of 3°C/s while holding the clamped device at the touch force.
- 3) Pressure stage – Once the desired assembly temperature was reached, the pressure was immediately increased to the optimum pressure of 680 kN/m^2 .
- 4) Holding stage – The assembly temperature and pressure were maintained for 900 s.
- 5) Cooling stage – Once assembly was complete, the temperature was gradually reduced to $\leq 35^\circ\text{C}$ at a rate of 1°C/s while holding the device at the assembly pressure. This reduced stress imposed on the cover plate and prevented collapse into the fluidic channels.
- 6) Demolding stage – After the assembled device was cooled, the platens were slowly withdrawn.

Water contact angle measurements. The wettability of the polymer surfaces, effect of plasma power and exposure time and the ageing of the cover plate were assessed by water contact angle measurements using a VCA Optima instrument (AST Products). A volume of $2.0 \mu\text{L}$ nanopure water ($18.2 \text{ M}\Omega\cdot\text{cm}$ at 25°C) was dispensed onto $1 \text{ cm} \times 1 \text{ cm}$ thermoplastic surfaces and a photograph of each droplet captured immediately for analysis using the software provided by the manufacturer. The measurements were repeated five times at different positions on the substrate with the values reported as the mean \pm one standard deviation.

Bond strength measurements. A common technique used to evaluate the bond strength is the double cantilever beam test also known as the crack opening method.^{37, 38} In this technique, a razor blade of known thickness t_b is inserted between the bonded substrate and cover plate inducing an interfacial fracture (or equilibrium crack) with a length L from the edge of the razor. If the elastic moduli of the substrate and cover plate is represented by E_s and E_p , respectively, the bond strength γ (J/cm²) defined by the interfacial surface energy is given by;

$$\gamma = \frac{3t_b^2 E_s t_s^3 E_p t_p^3}{16L^4 (E_s t_s^3 + E_p t_p^3)} \quad (1)$$

where t_s and t_p are the thicknesses of substrate and cover plate, respectively. In this work, all tests were performed using a stainless steel single edge razor blade with a thickness of 0.009" and the crack lengths were measured using a calibrated upright microscope with a 5× objective lens. Bond strengths were calculated using equation 1 with an elastic modulus of 3.3 GPa for PMMA, 2.60 GPa for COC 8007 and 3.0 GPa for COC 5010 as provided by the manufacturer. Measurements were performed in triplicate and values were plotted against the assembly temperature (°C), time (s) and pressure (N/m²).

Surface charge measurements. Direct current (DC) conductance measurements were used to evaluate the surface charge density in nanochannels. Conductance plots were generated using KCl solutions in the concentration range of 10⁻⁶ to 0.1 M KCl following procedures previously reported.^{34, 39} For UV/O₃ activation of the nanochannels, assembled devices were placed in a 265 nm UV chamber with the cover plate facing the light source and exposed to a 350 mJ/cm² of UV/O₃ light through the COC cover plate. In all cases, fluidic devices were initially flushed with methanol/ultrapure water (50% v/v) followed by rinsing with deionized water. Pre-cleaned devices were filled with KCl solutions with Ag/AgCl electrodes immersed into the access reservoirs poised at the ends of microchannels. Electrolyte solutions were allowed to equilibrate

for 3-5 min as evidenced by a stable current value under a fixed bias voltage. Current-voltage plots were generated by fitting the slope of the ionic current as a function of the applied voltage from -0.5 V to 0.5 V with 50 mV steps and a 5 s holding time at each step. All measurements were performed using the Axopatch 200B amplifier coupled to a Digidata 1440A digitizer with signal acquisition and analysis performed with the pClamp10 software. The average conductance generated from five trials was plotted against the electrolyte concentration in a log-log plot and the surface charge (σ_s) determined by fitting the graphs with the conductance equation,³⁴

$$G_T = 10^3 \left(\mu_{K^+} + \mu_{Cl^-} \right) c N_A e \cdot \frac{n w h}{L} + 2 \mu_{opp} \sigma_s n \frac{(w+h)}{L} \quad (2)$$

where G_T is the total measured conductance in the nanochannel, w , L and h are the nanochannel width, length and height, respectively, N_A is Avogadro's number, e is the electron charge (1.602×10^{-19} C), c is the electrolyte concentration in mol/L, n is the number of nanochannels in the device and μ_{K^+} and μ_{Cl^-} are the ion mobilities of K^+ and Cl^- ions, respectively ($\mu_{K^+} = 7.619 \times 10^{-8}$ m²/V s and $\mu_{Cl^-} = 7.912 \times 10^{-8}$ m²/V s) and $\mu_{opp} \approx \mu_{K^+}$ for the deprotonated carboxyl surface. Finally, we assessed the effects of electrolyte pH on the surface conductance using KCl solutions prepared over a pH range of 5 – 9 adjusted using HCl or KOH solutions.

Atomic Force Microscopy (AFM) and Scanning Electron Micrographs (SEMs). The topologies of the nanofluidic channels and the roughness of the polymer surfaces were investigated using an Asylum Research MFP-3D Atomic Force Microscope (tip radius ~2 nm) in repulsive tapping mode at a rate of 1.0 Hz. The Tap300A1-G cantilever tips (Ted Pella) had a frequency of 300 kHz and force constant of 40 N/m. For SEM, the non-conductive resin stamps and thermoplastic substrates were pre-coated with a 2-3 nm Au/Pd layer and imaged using a FEI Helios FIB/SEM.

Nanofluidic devices and DNA translocation. All fluorescence imaging experiments were performed using an inverted microscope (Olympus IX81 TIRF microscope, Olympus, Pennsylvania, PA) equipped with a 100×/1.49 NA oil immersion objective (WD = 0.19 mm) and 488 nm laser light for excitation, Sedat laser filter set (LF488/561-2X2M-B-000, Semrock) and a Hamamatsu EMCCD digital camera with Metamorph software for data acquisition. All images were analyzed using Fiji software. λ -DNA (Promega Corporation) and T4 DNA (Wako Chemicals) were stained with the bis-intercalating dye, YOYO-1 (Molecular Probes, Eugene, OR) at a base-pair/dye ratio of 5:1 in a buffer solution of 1× TBE (89 mM Tris, 89 mM Borate, 1 mM EDTA) with the addition of 4% v/v β -mercaptoethanol used as a radical scavenger to minimize photo-induced damage (photobleaching and/or photonicking).

Nanofluidic channels with sizes between 25 and 300 nm were fabricated in PMMA and assembled using the scheme previously described (see Fig. 1b). Devices were seeded with 5 mM FITC in 1× TBE and allowed to equilibrate for 3 min before imaging through the thin COC cover plate at an exposure time of 2 s using an inverted fluorescence microscope (device was placed on the microscope stage with the cover plate facing the objective). Unprocessed images were imported into Fiji software and the fluorescence SNR was computed for each nanofluidic channel using the relation;⁴⁰

$$\text{SNR} = 0.655 \frac{S_{\text{avg}}}{\sigma_{\text{noise}}} \quad (3)$$

where S_{avg} is the mean pixel intensity of the signal (background corrected) and σ_{noise} is the standard deviation in the background pixel intensity. The factor of 0.655 arises because of the (Gaussian) noise.⁴⁰

We investigated the degree of extension of T4-DNA molecules confined in nanochannels designed with a range of predefined sizes. The DNA molecules were driven from the

microchannels into the nanochannel under low field strengths. Once they had fully entered the nanochannel, the DC field was switched off. The molecule was allowed to relax until it reached its equilibrium extension length before an image was acquired. The end-to-end distance of the fluorescence image was measured using Fiji software. Although the total contour length (L_c) of an unstained T4-DNA molecule (166 kbp) is $\sim 56.6 \mu\text{m}$, at our intercalating dye concentration the expected length is $\sim 64 \mu\text{m}$.⁴¹ Finally, the velocities of λ -DNA molecules (0.75 pM) electrokinetically driven through an untreated and UV/O₃-activated hybrid device was evaluated from time-lapse images acquired at 120 fps.

RESULTS AND DISCUSSIONS

Water contact angle measurements. In a typical nanofluidic device assembly process, the maximum bond strength between the substrate and cover plate is in part a function of the difference in hydrophobicity/hydrophilicity of the surfaces that are in contact. In our initial bonding tests performed using a low T_g untreated COC cover plate and a high T_g untreated substrate, we were only able to achieve bonding when the devices were assembled at temperatures greater than the T_g of the cover plate by 5°C or more (data not shown). However, at these temperatures the nanochannels showed significant deformation and the cover plate collapsed, rendering the device nonfunctional. Therefore, before device assembly O₂ plasma was used to pre-activate the COC cover plate to make it more hydrophilic and thus, improve its adhesion to a PMMA substrate, which was not plasma treated.

It is well-established that O₂ plasma generates oxygen-containing polar functional groups on thermoplastic surfaces by inducing free radical reactions between the polymer chains and atomic oxygen in the plasma.^{42, 43} Also, as the plasma power and treatment times are increased, the surface not only becomes richer in oxygen-containing groups but rougher as well. The RMS

roughness can result in distortions of the electroosmotic flow (EOF) in nanochannels, especially when the ratio of the RMS roughness to the electric double layer (EDL) thickness ≥ 1 .³⁹ For these reasons, water contact angle and AFM measurements were used to assess the hydrophilicity and surface roughness, respectively, for determining the optimum O₂ plasma RF power and exposure time for treating the COC cover plate.

Fig. 2a shows the relationship between the water contact angle and the plasma power at a 10 s exposure time (O₂ gas flow rate = 10 sccm). As shown, O₂ plasma treatment resulted in a decrease in the water contact angle; $96 \pm 2^\circ$ for the untreated COC surface to $47 \pm 1^\circ$ and $45 \pm 1^\circ$ for surfaces treated at 20 W and 80 W RF power, respectively, indicating an increase in the surface energy.⁴³ The black trace in Fig. 2b shows the variation of the water contact angle with an exposure time in the range of 6 to 60 s at 50 W plasma power. As can be seen, there was a decrease in the water contact angle from $46 \pm 1^\circ$ to $42 \pm 1^\circ$ when the treatment time was increased from 6 s to 30 s. Above 30 s, the water contact angle slightly decreased to a constant value of $41 \pm 1^\circ$. As shown in Fig. 2c (blue trace), the surface roughness increased almost linearly from 0.49 ± 0.03 nm for the untreated COC surface to 1.06 ± 0.06 nm for the surface treated for 60 s. From these results, we used O₂ plasma conditions of 50 W RF power with a 30 s exposure time and a 10 sccm oxygen flow rate to treat the COC cover plate to maximize the surface energy while minimizing surface roughness. Because the EDL thickness for most ionic solutions used in nanofluidics varies between 1-100 nm and the RMS roughness of the COC surface treated at the above plasma condition was low (0.62 ± 0.04 nm), we speculate that distortions in the EOF profile arising from the surface roughness associated with the nanochannel would be minimal.

Although the surface properties of thermoplastics can be modified by plasma treatment without affecting its bulk properties, treated surfaces have been shown to undergo ageing when

stored in air. This is due to reorientation of the polar surface functional groups causing their movement into the bulk thermoplastic and, thus, loss of the hydrophilic character.^{39, 44} Ageing studies were performed on treated COC cover plates to determine if assembled nanofluidic devices could be stored. The results obtained after treating the COC cover plate with 50 W RF power and 30 s exposure time are shown in Fig. 2c. These results revealed that the contact angle changed from $41 \pm 1^\circ$ to $53 \pm 1^\circ$ during the first 10 h following treatment. Over a period of 100 h, the contact angle remained at $56 \pm 1^\circ$. The hydrophilicity was not completely lost over the storage time evaluated as the contact angle was still 35-40° lower than that of the untreated COC surface. Also, we did not experience any difficulty in filling devices used 5 d after assembly and these devices yielded results similar to those obtained from devices that were used immediately after assembly.

Because we were interested in post-assembly modification of the nanochannels by UV/O₃-activation through the COC cover plate, we assessed the wettability of a PMMA substrate before and after exposure to UV light with and without a COC cover plate. We used U-, PL- and UV- prefixes to indicate untreated, plasma treated and UV/O₃-activated surfaces, respectively, and represented assembled devices as 'substrate/(cover plate)'. For example, an untreated PMMA substrate bonded to an O₂ plasma treated COC cover plate was represented as 'U-PMMA/(PL-COC)'. As can be seen in Fig. 2d, U-PMMA showed a water contact angle of $68 \pm 3^\circ$. Direct exposure to RF O₂ plasma under the above conditions resulted in a decrease in the contact angle to $49 \pm 2^\circ$. However, direct exposure to 350 mJ/cm² of UV/O₃ light resulted in a reduction in the contact angle to $25 \pm 1^\circ$ with an observed yellowing of the polymer. When the PMMA substrate was activated through an untreated PMMA cover plate, the water contact angle was $66 \pm 2^\circ$, a value similar to that obtained for U-PMMA. This was not surprising considering that PMMA has

been shown to transmit 10-15% of light at a wavelength of 265 nm.³¹ The measured contact angles for U-PMMA/(U-COC) and U-PMMA/(PL-COC) were $48 \pm 1^\circ$ and $47 \pm 2^\circ$, respectively; these contact angles were not statistically different but were lower than U-PMMA by 15-20°. These results revealed that PMMA substrates could be successfully activated through a COC cover plate by UV/O₃ light and also that plasma treatment of the cover plate had no considerable effect on the bulk transmittance of the material because it only affects 5-15 nm of the polymer below its surface.⁴³

Bond strength determinations. The critical parameters in any fusion bonding scheme adopted for enclosing fluidic devices are the bonding pressure, temperature and time. We optimized these parameters to obtain high bond strengths while retaining the structural integrity of the nanofluidic channels. Before device assembly, the COC cover plate was treated with oxygen plasma consisting of 50 W RF power for 30 s and 10 sccm gas flow rate while the PMMA substrate remained untreated. Variations between the bonding temperature and the bond strength at a constant bonding pressure of 680 kN/m² and a bonding time of 15 min are shown in Fig. 3a. The results revealed that the bond strength varied linearly with the bonding temperature. Based on the work of Tsao *et al.*,³⁸ bond strengths for our nanofluidic devices were comparable to those of microfluidic devices. Our data revealed that bonding at 80°C resulted in unusable devices. This is likely a result of bulk flow of the cover plate material into the nanochannels due to the bonding temperature being greater than its bulk T_g. In subsequent studies, 70°C was selected as the optimal bonding temperature.

Next, we studied the effects of assembly time on the bond strength using the optimal temperature of 70°C and a constant force of 680 kN/m². As shown in Fig. 3b, bond strengths were greater than those previously reported in thermoplastic nanochannels.^{15, 34} We observed that

devices bonded at 20 min did not yield reproducible results. We speculate that this may be due to deformations in the nanochannels or sagging of the cover plate into the channels similar to previous observations.³⁰ Therefore, 15 min was selected as the optimal assembly time.

Lastly, Fig. 3c shows the effect of bonding pressure on the bond strength using an optimal bonding temperature of 70°C and a bonding time of 15 min. Bond strengths achieved in the pressure range under study were sufficiently greater than that previously reported for electrokinetic flow in nanofluidic devices¹⁵ and comparable to the same polymer used as the cover plate and substrate and bonded at a temperature greater than their T_g .³⁸ Therefore, to prevent sagging of the cover plate into the nanochannels, we selected 680 kN/m² as the optimum pressure. Based on the aforementioned results, untreated high T_g substrates were bonded to O₂ plasma treated low T_g COC cover plates using a bonding pressure, temperature and time of 680 kN/m², 70°C and 15 min, respectively.

Similarly, we evaluated the bond strengths for devices comprising of PL-PMMA, U-COC ($T_g = 108^\circ\text{C}$) and PL-COC ($T_g = 108^\circ\text{C}$) substrates bonded to PL-COC ($T_g = 75^\circ\text{C}$). The results are summarized in Table 1. Devices 1 – 4 were bonded at the optimized bonding pressure, temperature and time as previously noted. Device 5 was bonded using a pressure of 370 kN/m² at 80°C for ~7 min as previously reported by our group.³⁴ Device 1 (U-COC/(PL-COC)) produced a bond strength that was too low for performing fluidic experiments because we experienced difficulty in filling the assembled device; filling caused delamination of the cover plate from the substrate. Using PMMA as the substrate produced devices with bond strengths of $66 \pm 7 \text{ mJ/cm}^2$ and $68 \pm 7 \text{ mJ/cm}^2$ for U-PMMA/(PL-COC) and PL-PMMA/(PL-COC), respectively, that easily filled by capillary action. Though it remains unclear why the bond strength was greater in U-PMMA/(PL-COC) than PL-COC/(PL-COC), we concluded from these results that the bond

strength not only depends on the surface wettability – PL-COC has a water contact angle less than U-PMMA – but also on the chemical nature of the surfaces in contact. Nevertheless, U-PMMA/(PL-COC) devices, which we refer to as the hybrid devices, were used in our subsequent experiments due to their high bond strengths.

For comparison, we evaluated the bond strengths from assembled PL-PMMA/(PL-PMMA) and U-PMMA/(U-PMMA) devices. As shown in Table 1, in both cases, the measured bond strengths were lower than that of the hybrid devices. Though PL-PMMA/(PL-PMMA) devices have been used for DNA transport studies,^{15, 16, 34} the process yield rate for both devices was relatively low (<50% for PL-PMMA/(PL-PMMA) and <10% for U-PMMA/(U-PMMA)) due primarily to deformation and collapse of the nanochannels following thermal fusion bonding and possible delamination of the cover plate during an experiment.¹⁵ As a comparison, using the optimized thermal fusion bonding conditions noted above for U-PMMA/(PL-COC) devices, the process yield rate was >90% with a similar value noted for devices consisting of U-COC/(PL-COC). AFM measurements taken from the 5 μm \times 120 nm nanoslits, after removing the cover plate, revealed no change in the nanoslit dimensions. This was not surprising because device assembly was performed at a temperature $\sim 35^\circ\text{C}$ less than the T_g of the PMMA substrate.

Surface charge measurements. We recently reported the surface charge density in PL-PMMA/(PL-PMMA) nanofluidic devices assembled under different plasma conditions (5.5 sccm, 35 s and 50 W).³⁴ Herein, we evaluated the surface charge density of hybrid U-PMMA/(PL-COC) devices assembled with the optimum conditions reported above.

Ionic conductance plots were used to evaluate the surface charge density of assembled nanofluidic devices consisting of an array of 5 nanoslits each 5 μm wide, 120 nm deep and 148 μm long. It is well-known that carboxylic acid moieties can be generated on PMMA or COC

surfaces following O_2 plasma treatment^{39, 44} or UV/ O_3 -activation.⁴⁵ Fig. 4a shows the conductance traces measured in PL-PMMA/(PL-COC) compared to PL-PMMA/(PL-PMMA) devices. In the high ionic strength regime (KCl concentrations $>10^{-2}$ M), the ionic conductance in both devices fit linearly to the theoretical bulk conductance with high reproducibility for both devices. This confirmed that there was no change in the dimensions of the nanochannels during thermal embossing and after assembly. At the low ionic concentration (or surface-charge governed) regime, there was a significant difference in the measured conductance between these devices. For the PL-PMMA/(PL-PMMA) device, the surface charge density $|\sigma_s|$ estimated from the fitted curve was 43.2 mC/m^2 while for the hybrid device, $|\sigma_s|$ was 57.3 mC/m^2 , $\sim 32.6\%$ greater than the former. This difference in $|\sigma_s|$ was likely due to the fact that more carboxyl groups are generated on COC compared to PMMA when treated under similar O_2 plasma conditions.^{39, 44}

Fig. 4b shows the conductance traces measured in the hybrid device U-PMMA/(PL-COC) before (blue trace) and after (red trace) exposure to UV/ O_3 light. The average conductance in the low ionic strength regime for the unexposed devices was $1.45 \times 10^{-9} \text{ S}$ with $|\sigma_s|$ equal to 40.7 mC/m^2 . After the device was exposed to 350 mJ/cm^2 of 265 UV light through the plasma-treated COC cover plate, there was a 47.2% increase in $|\sigma_s|$ (59.9 mC/cm^2) as evidenced by the increase in conductance to $1.89 \times 10^{-9} \text{ S}$. This suggested that post-assembly UV/ O_3 activation induced more carboxyl groups on the walls of the nanoslits, in particular for the unmodified PMMA substrate. Also, the surface charge density in the UV/ O_3 activated hybrid devices were 4.5% higher than devices with an O_2 plasma treated substrate (red trace in Fig. 4a). This is because the surface density of carboxylates generated on UV/ O_3 activated PMMA surfaces ($15 \pm 3 \text{ nmol/cm}^2$)⁴⁵ is greater than that generated on plasma treated surfaces ($3 \pm 1 \text{ nmol/cm}^2$).⁴⁶

Fig. 4c shows the effects of solution pH on the measured conductance for the nanoslits before and after UV/O₃ activation. As can be seen, in both cases the conductance increased linearly with the pH of the electrolyte. Prior to UV/O₃ activation, there was an observed change in the measured conductance of the nanochannel from $13.7 (\pm 0.2) \times 10^{-10}$ S at pH 5.0 to $15.5 (\pm 0.5) \times 10^{-10}$ S at pH 9.1 (black trace). Because the PMMA substrate was untreated prior to device assembly, charge contributions from carboxyl moieties on the PMMA surfaces, especially at high pH, will be insignificant compared to that from the plasma treated COC cover plate. Therefore, this change in conductance is predominantly due to deprotonation of the carboxyl groups on the cover plate. Nevertheless, after UV/O₃-activation of the same devices, there was a significant increase in the conductance, ~30% ($15.4 (\pm 0.4) \times 10^{-10}$ S at pH 5.0 to $\sim 21.6 (\pm 0.6) \times 10^{-10}$ S at pH 9.1), as evident by an increase in the slope of the red trace in Fig. 4c. These results confirmed that the nanoslits were successfully UV/O₃ activated after device assembly.

Operational characteristics of hybrid nanofluidic devices. We assessed the performance of assembled hybrid nanofluidic devices for fluorescence imaging, DNA stretching and translocation relative to their non-hybrid counterparts. Fig. 5a shows an AFM profile and the SEM image (insert) of the UV curable resin stamp consisting of 2-D nanochannels was used to imprint channels into a PMMA substrate with ~100% replication fidelity (see Fig. S1 and S2 in the SI). The dimensions of these nanochannels was, widths (w) \times depths (d), 300×200 nm, 250×155 nm, 190×95 nm, 150×60 nm, 110×25 nm and 35×35 nm (see Fig. S3a – d in SI for SEMs) corresponding to $nc1$, $nc2$, $nc3$, $nc4$, $nc5$, and $nc6$, respectively. Using unprocessed images obtained from a seeding test using 5 mM FITC, and a selected area of $18 \mu\text{m}^2$ in all cases, we found that the average SNR was $\sim 3\times$ greater in $nc1 - nc4$ and $\sim 4.5\times$ greater in $nc5$ for U-PMMA/(PL-COC) compared to PL-PMMA/(PL-PMMA) devices (Fig. 5b). The measured

σ_{noise} under these imaging conditions were 2.6 and 5.8 for U-PMMA/(PL-COC) and PL-PMMA/(PL-PMMA) devices, respectively. The enhancement in the SNR for the hybrid devices was most likely due to the superior optical properties of COC at 488 nm compared to PMMA.³¹ The higher SNR observed for *nc5* may be an indication of collapse of the nanochannel in the non-hybrid devices and/or an artifact from the high background fluorescence of PMMA.

Fig. 5c shows unprocessed frames of T4 DNA molecules confined in *nc1* – *nc6* devices (U-PMMA/(PL-COC)) and imaged through the cover plate at 10 ms exposure time. The images revealed good contrast and excellent SNR with the degree of polymer stretching increasing as the nanochannel size decreased. Fig. 5d shows a plot of the DNA extension (ϵ) versus the geometric average (D_{av}) nanochannel dimension with traces for the deGennes, $\epsilon_{deGennes} \approx (\omega_{eff} L_p / D_{av}^2)^{1/3}$ and the Odijk, $\epsilon_{Odijk} \approx [1 - 0.361(D_{av}/L_p)^{2/3}]$ regimes, where $D_{av} = \sqrt{w \times d}$, with ω_{eff} being the effective width (~ 3 nm) and L_p is the persistence length (50 nm) for dsDNA.⁴¹ As seen in Fig. 5d, the data for the channel with >200 nm D_{av} fits well with the deGennes regime while the nanochannel with $D_{av} = 35$ nm fits well to the Odijk regime. However, data for *nc3* – *nc5*, though expected to fit to the deGennes regime, were observed to be greater than the deGennes prediction but less than the Odijk prediction. The failure of fit in this size regime could have resulted from the degree of extension partly arising from the surface energy of the nanochannel walls.⁴⁷

Finally, we evaluated the effect of post-assembly UV/O₃-activation of the U-PMMA/(PL-COC) devices on the linear velocity of λ -DNA molecules electrokinetically driven through 100×100 nm nanochannels. As shown in Fig. 6, in both cases there was a corresponding linear increase in the velocity of dsDNA as the driving voltage was increased. However, the DNA molecules were observed to migrate slower in the UV/O₃-activated devices. This was likely due

to an increase in the EOF emanating from increases in the surface charge density that occurs due to UV/O₃ activation.

CONCLUSION

In this work, we have developed a low temperature hybrid bonding scheme for the assembly of thermoplastic devices with high process yield rates and demonstrated the utility of these devices for DNA elongation and translocation as well as post-assembly activation of the nanochannels using UV/O₃ light. With the reported assembly process, we have addressed a significant challenge associated with the use of thermoplastics for nanofluidics – the relatively small Young's modulus associated with these materials makes cover plate assembly to the patterned substrate difficult due to cover plate collapse and/or nanostructure deformation using thermal or solvent-assisted bonding to enclose the fluidic network. Our hybrid assembly scheme generates nanofluidic devices with high process yield rates (>90%) even for devices with channel dimensions of 35 nm using a relatively short processing time (16 min). While the reported bonding scheme was restricted to thermoplastics, it can be envisioned for non-thermoplastic substrates as well. For example, we have found that PL-COC cover plates can be thermally fusion bonded to nanofluidic devices composed of fused silica substrates using the same scheme as shown in Fig. 1b with similar process yield rates (data not shown). For comparison, we found that bonding fused silica cover plates to fused silica substrates generated a process yield rate of 60 – 70% using a class 1000 cleanroom following similar procedures as outlined by Suni *et al.*³⁵

We are currently evaluating the extent of distortions in the EOF profile, if any, arising from hybrid nanofluidic channels as has been shown in microchannels.⁴⁸ We suspect these distortions will be observed in PL-COC/(PL-COC) devices as well due to differences in the norbornene content of the substrate versus cover plate. We will be employing super-resolution imaging to

assess the surface coverage and uniformity of carboxyl groups generated in these nanofluidic channels via UV-activation and also to study the distortions in the flow profile of the EOF.

ACKNOWLEDGEMENTS

The authors would like to thank the National Institute of Health (NIH R21HG006278) and the National Science Foundation (CBET-1067583) for support of this work. We also thank the UNC Chapel Hill Analytical and Nanofabrication Laboratory and the UNC-Olympus Imaging Research Center for their assistance in device fabrication and imaging.

REFERENCES

1. S. Prakash, A. Piruska, E. N. Gatimu, P. W. Bohn, J. V. Sweedler and M. A. Shannon, *Sensors Journal, IEEE*, 2008, 8, 441-450.
2. P. Abgrall and N. T. Nguyen, *Analytical Chemistry*, 2008, 80, 2326-2341.
3. J. Han, S. W. Turner and H. G. Craighead, *Physical Review Letters*, 1999, 83, 1688-1691.
4. T. Odijk, *Physical Review E*, 2008, 77, 060901.
5. L. J. Guo, X. Cheng and C.-F. Chou, *Nano Letters*, 2003, 4, 69-73.
6. W. Reisner, *Physical Review Letters*, 2005, 94, 196101.
7. W. Reisner, J. P. Beech, N. B. Larsen, H. Flyvbjerg, A. Kristensen and J. O. Tegenfeldt, *Physical Review Letters*, 2007, 99, 058302.
8. S. Fang Lim, A. Karpusenko, J. J. Sakon, J. A. Hook, T. A. Lamar and R. Riehn, *Biomicrofluidics*, 2011, 5.
9. R. Riehn, M. Lu, Y.-M. Wang, S. F. Lim, E. C. Cox and R. H. Austin, *Proceedings of the National Academy of Sciences of the United States of America*, 2005, 102, 10012-10016.
10. M. Foquet, J. Korlach, W. Zipfel, W. W. Webb and H. G. Craighead, *Analytical Chemistry*, 2002, 74, 1415-1422.
11. W. Li, *Nanotechnology*, 2003, 14, 578-583.
12. J. Tegenfeldt, C. Prinz, H. Cao, R. Huang, R. Austin, S. Chou, E. Cox and J. Sturm, *Anal Bioanal Chem*, 2004, 378, 1678-1692.
13. R. Chantiwas, S. Park, S. A. Soper, B. C. Kim, S. Takayama, V. Sunkara, H. Hwang and Y.-K. Cho, *Chemical Society Reviews*, 2011, 40, 3677-3702.
14. S. Y. Chou, P. R. Krauss and P. J. Renstrom, *Applied Physics Letters*, 1995, 67, 3114-3116.
15. R. Chantiwas, M. L. Hupert, S. R. Pullagurla, S. Balamurugan, J. Tamarit-Lopez, S. Park, P. Datta, J. Goettert, Y.-K. Cho and S. A. Soper, *Lab on a Chip*, 2010, 10, 3255-3264.
16. J. Wu, R. Chantiwas, A. Amirsadeghi, S. A. Soper and S. Park, *Lab on a Chip*, 2011, 11, 2984-2989.
17. P. Abgrall, L.-N. Low and N.-T. Nguyen, *Lab on a Chip*, 2007, 7, 520-522.
18. P. E. Shao, A. van Kan, L. P. Wang, K. Ansari, A. A. Bettioli and F. Watt, *Applied Physics Letters*, 2006, 88, -.

19. P. Sivanesan, K. Okamoto, D. English, C. S. Lee and D. L. DeVoe, *Analytical Chemistry*, 2005, 77, 2252-2258.
20. J.-M. Li, C. Liu, X. Ke, Y.-j. Duan, Y. Fan, M. Li, K.-p. Zhang, Z. Xu and L.-d. Wang, *Microsyst. Technol.*, 2013, 19, 1845-1850.
21. E. Cheng, H. Zou, Z. Yin, P. Jurcicek and X. Zhang, *J. Micromech. Microeng.*, 2013, 23.
22. L. Junshan, Q. Hongchao, X. Zheng, L. Chong, W. Junyao, D. Liqun, Z. Xi and W. Liding, *Micro & Nano Letters, IET*, 2012, 7, 159-162.
23. J. Liu, X. Jin, T. Sun, Z. Xu, C. Liu, J. Wang, L. Chen and L. Wang, *Microsyst. Technol.*, 2013, 19, 629-634.
24. J.-m. Li, C. Liu, X. Ke, Z. Xu, Y.-j. Duan, Y. Fan, M. Li, K.-p. Zhang and L.-d. Wang, *Lab on a Chip*, 2012, 12, 4059-4062.
25. L. Zhang, F. Gu, L. Tong and X. Yin, *Microfluid. Nanofluid.*, 2008, 5, 727-732.
26. Y. H. Cho, J. Park, H. Park, X. Cheng, B. J. Kim and A. Han, *Microfluid. Nanofluid.*, 2010, 9, 163-170.
27. H. T. Lasse, K. Anna and K. Anders, *Nanotechnology*, 2008, 19, 125301.
28. X. Hu, Q. He, X. Zhang and H. Chen, *Microfluid. Nanofluid.*, 2011, 10, 1223-1232.
29. B. Bilenberg, M. Hansen, D. Johansen, V. Özkapici, C. Jeppesen, P. Szabo, I. M. Obieta, O. Arroyo, J. O. Tegenfeldt and A. Kristensen, *Journal of Vacuum Science & Technology B*, 2005, 23, 2944-2949.
30. E. Cheng, Z. Yin, H. Zou and L. Chen, *Microfluidics and Nanofluidics*, 2014, 1-9.
31. A. Piruska, I. Nikcevic, S. H. Lee, C. Ahn, W. R. Heineman, P. A. Limbach and C. J. Seliskar, *Lab on a Chip*, 2005, 5, 1348-1354.
32. G. Khanarian and H. Celanese, *OPTICE*, 2001, 40, 1024-1029.
33. R. Jena, C. Y. Yue and Y. C. Lam, *Microsyst. Technol.*, 2012, 18, 159-166.
34. F. I. Uba, S. Pullagurla, N. Sirasunthorn, J. Wu, S. Park, R. Chantiwas, Y.-K. Cho, H. Shin and S. A. Soper, *Analyst*, 2014, 139.
35. T. Suni, K. Henttinen, I. Suni and J. Mäkinen, *Journal of The Electrochemical Society*, 2002, 149, G348-G351.
36. Q. Y. Tong and U. Gösele, *Journal of The Electrochemical Society*, 1996, 143, 1773-1779.
37. P. Ramm, J. J.-Q. Lu and M. M. Taklo, *Handbook of Wafer Bonding*, John Wiley & Sons, 2012.

38. C. W. Tsao, L. Hromada, J. Liu, P. Kumar and D. L. DeVoe, *Lab on a Chip*, 2007, 7, 499-505.
39. A. Vesel and M. Mozetic, *Vacuum*, 2012, 86, 634-637.
40. M. J. Firbank, A. Coulthard, R. M. Harrison and E. D. Williams, *Physics in Medicine and Biology*, 1999, 44, N261.
41. W. Reisner, K. J. Morton, R. Riehn, Y. M. Wang, Z. Yu, M. Rosen, J. C. Sturm, S. Y. Chou, E. Frey and R. H. Austin, *Physical Review Letters*, 2005, 94, 196101.
42. J. Chai, F. Lu, B. Li and D. Y. Kwok, *Langmuir*, 2004, 20, 10919-10927.
43. S.-J. Hwang, M.-C. Tseng, J.-R. Shu and H. Her Yu, *Surface and Coatings Technology*, 2008, 202, 3669-3674.
44. S. Roy, C. Y. Yue, Y. C. Lam, Z. Y. Wang and H. Hu, *Sensors and Actuators B: Chemical*, 2010, 150, 537-549.
45. J. M. Jackson, M. A. Witek, M. L. Hupert, C. Brady, S. Pullagurla, J. Kamande, R. D. Aufforth, C. J. Tignanelli, R. J. Torphy, J. J. Yeh and S. A. Soper, *Lab on a Chip*, 2014, 14, 106-117.
46. F. Xu, P. Datta, H. Wang, S. Gurung, M. Hashimoto, S. Wei, J. Goettert, R. L. McCarley and S. A. Soper, *Analytical Chemistry*, 2007, 79, 9007-9013.
47. D. Bensimon, A. J. Simon, V. Croquette and A. Bensimon, *Physical Review Letters*, 1995, 74, 4754-4757.
48. D. Ross, T. J. Johnson and L. E. Locascio, *Analytical Chemistry*, 2001, 73, 2509-2515.

Table 1. A summary of the bond strengths for devices assembled with different substrates and cover plates. (U – untreated; PL – plasma treated and the material in parentheses is the cover plate). The number in [] is the assembly temperature used for that particular device.

Number	Assembled device	Bond Strength (mJ/cm^2)
1	U-COC/(PL-COC)	0.14 \pm 0.07
2	PL-COC/(PL-COC)	1.03 \pm 0.01
3	U-PMMA/(PL-COC)	66 \pm 7
4	PL-PMMA/(PL-COC)	67 \pm 7
5	PL-PMMA/(PL-PMMA) [80°C]	1.24 \pm 0.01
6	U-PMMA/(U-PMMA) [106°C]	1.90 \pm 0.05

LIST OF FIGURES

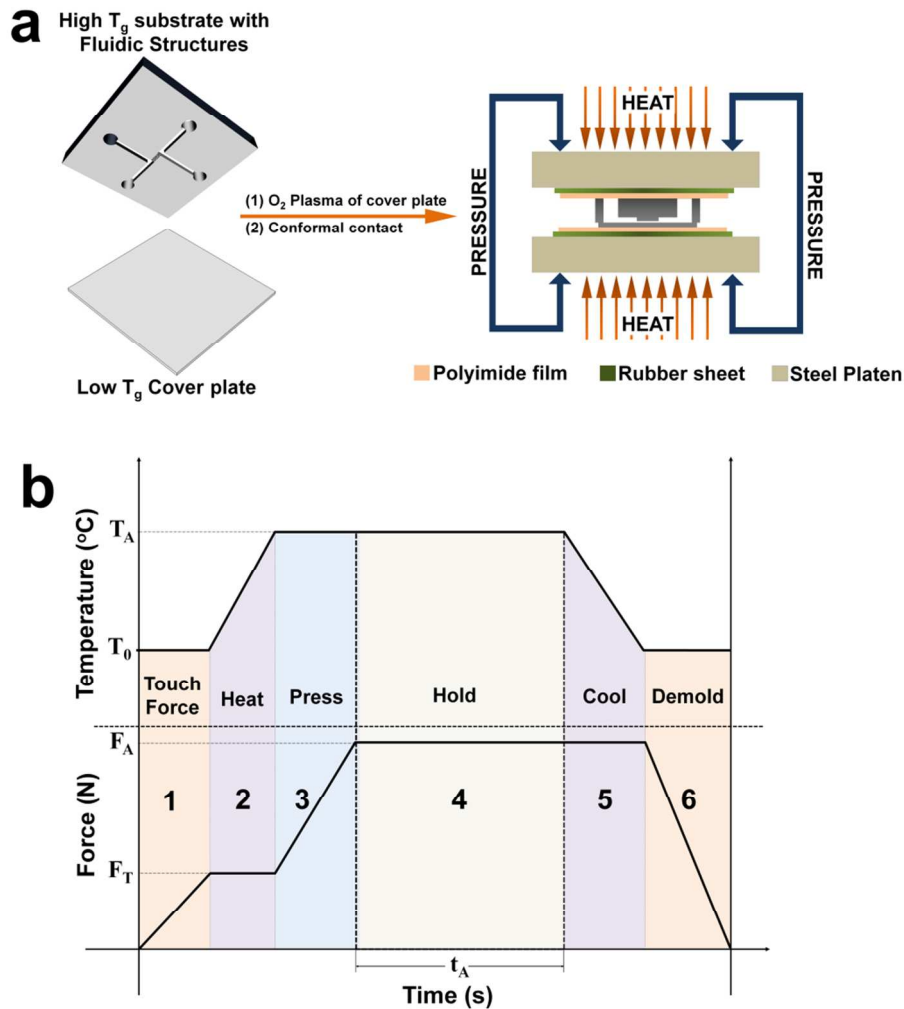


Figure 1. (a) Schematic of the protocol used for assembly of the hybrid-based fluidic devices and the thermal press instrument. (b) Temperature-pressure process profile showing the six stages for the thermal fusion bonding cycle. See main text for a description of the 6 stages of bonding.

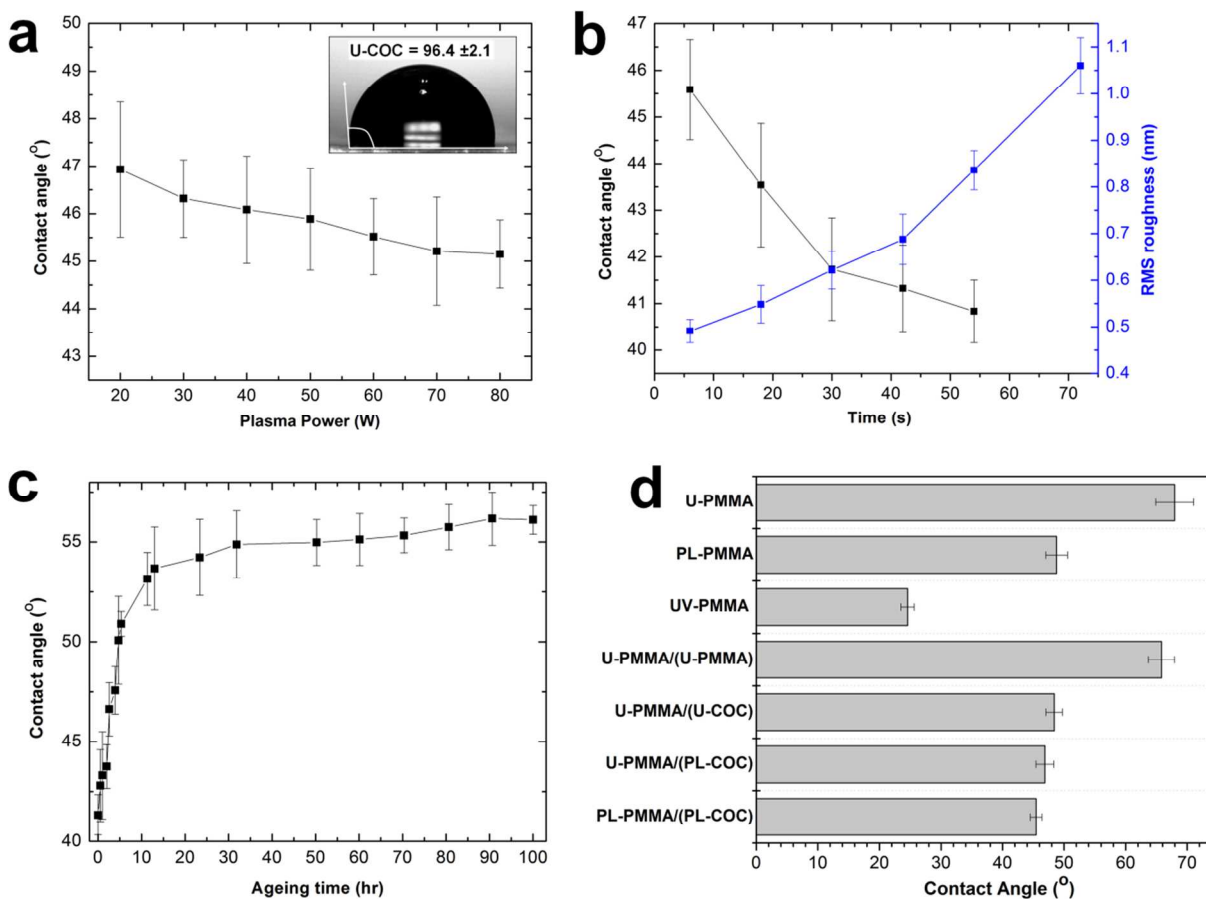


Figure 2. (a) Plot of the variation of the water contact angle with the RF power for an oxygen plasma at 10 sccm gas flow rate and a constant exposure time of 10 s. (b) Plot of the relationship between the water contact angle (black trace) and the RMS roughness (blue trace) versus the plasma exposure time at 50 W for 10 sccm O_2 gas flow rate. (c) Effect of ageing under room temperature conditions on the water contact angle of a plasma treated COC cover plate for plasma treatment of 50 W at 30 s under 10 sccm oxygen flow rate. (d) Water contact angle measurements of a PMMA substrate under different surface modification conditions with and without the COC cover plate. ‘U-PMMA’ is an untreated PMMA substrate; PL-PMMA is a plasma treated PMMA substrate; UV-PMMA is UV/ O_3 -activated PMMA substrate; U-PMMA/(U-PMMA) is untreated PMMA substrate UV/ O_3 -activated through an untreated PMMA cover plate; U-PMMA/(U-COC) is an untreated PMMA substrate UV-activated through an untreated COC cover plate; U-PMMA/(PL-COC) is untreated PMMA substrate UV-activated through a plasma treated COC cover plate; and PL-PMMA/(PL-COC) is plasma treated PMMA substrate UV/ O_3 -activated through a plasma treated COC cover plate.

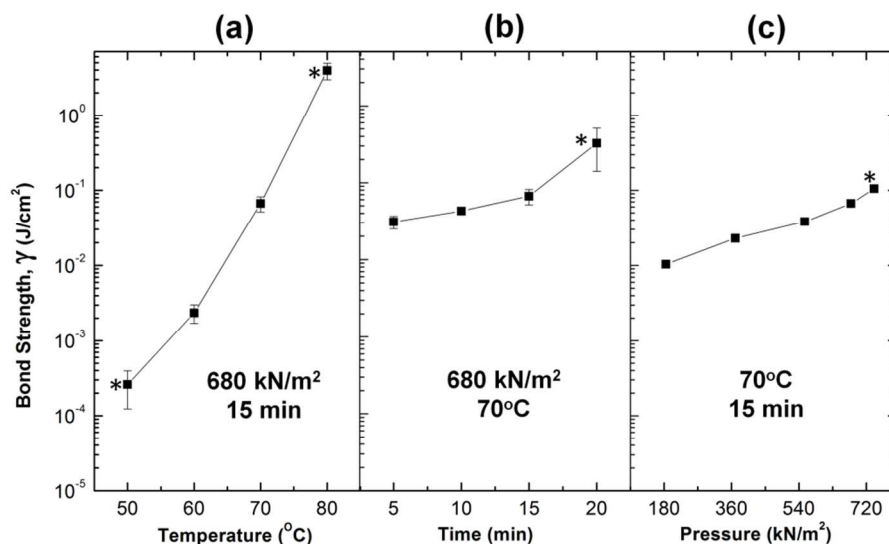


Figure 3. Variation of the bond strength with (a) temperature, (b) bonding time, and (c) pressure for the hybrid assembly scheme. The data points with the asterisks represent devices that were unusable due to the following reasons; delamination of the cover plates in the devices bonded at 50°C, refilling of the nanochannels by cover plate material in devices bonded at 80°C and irreproducibility of the experimental results as a result of nanochannel deformation or cover plate sagging in the devices bonded at high bonding time (20 min) and high bonding pressure (720 kN/m²).

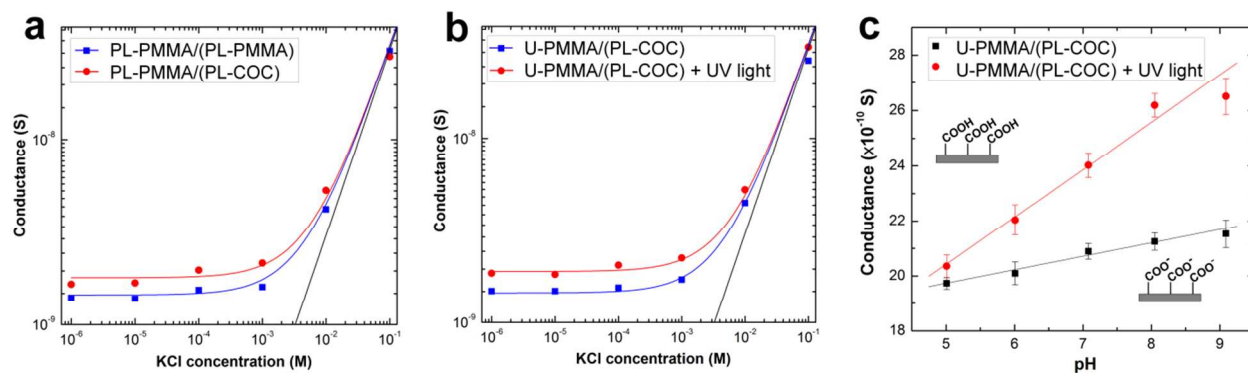


Figure 4. (a) Conductance plots for assembled devices with a plasma treated PMMA substrate bonded to a plasma treated PMMA cover plate, PL-PMMA/(PL-PMMA), and plasma treated PMMA substrate bonded to a plasma treated COC cover plate, PL-PMMA/(PL-COC). (b) Conductance plots for hybrid devices consisting of an untreated PMMA substrate bonded to a plasma treated COC cover plate, U-PMMA/(PL-COC), before (blue trace) and after (red trace) UV/O₃ activation. The devices used in all cases consisted of an array of five nanoslits (5 μm wide, 120 nm deep and 148 μm long) connected to V-shaped access microchannels at the input and output ends. Each data point represents an average of five measurements with scatter in the data within 5-8% of the mean value. The solid black line represents the trace of the theoretical bulk conductance. (c) Plot showing the relationship between the conductance and the electrolyte pH for assembled hybrid devices before (black) and after (red) UV/O₃ activation. 10⁻⁴ M KCl solution adjusted to a pH between 5.0 and 9.1 was used in the study.

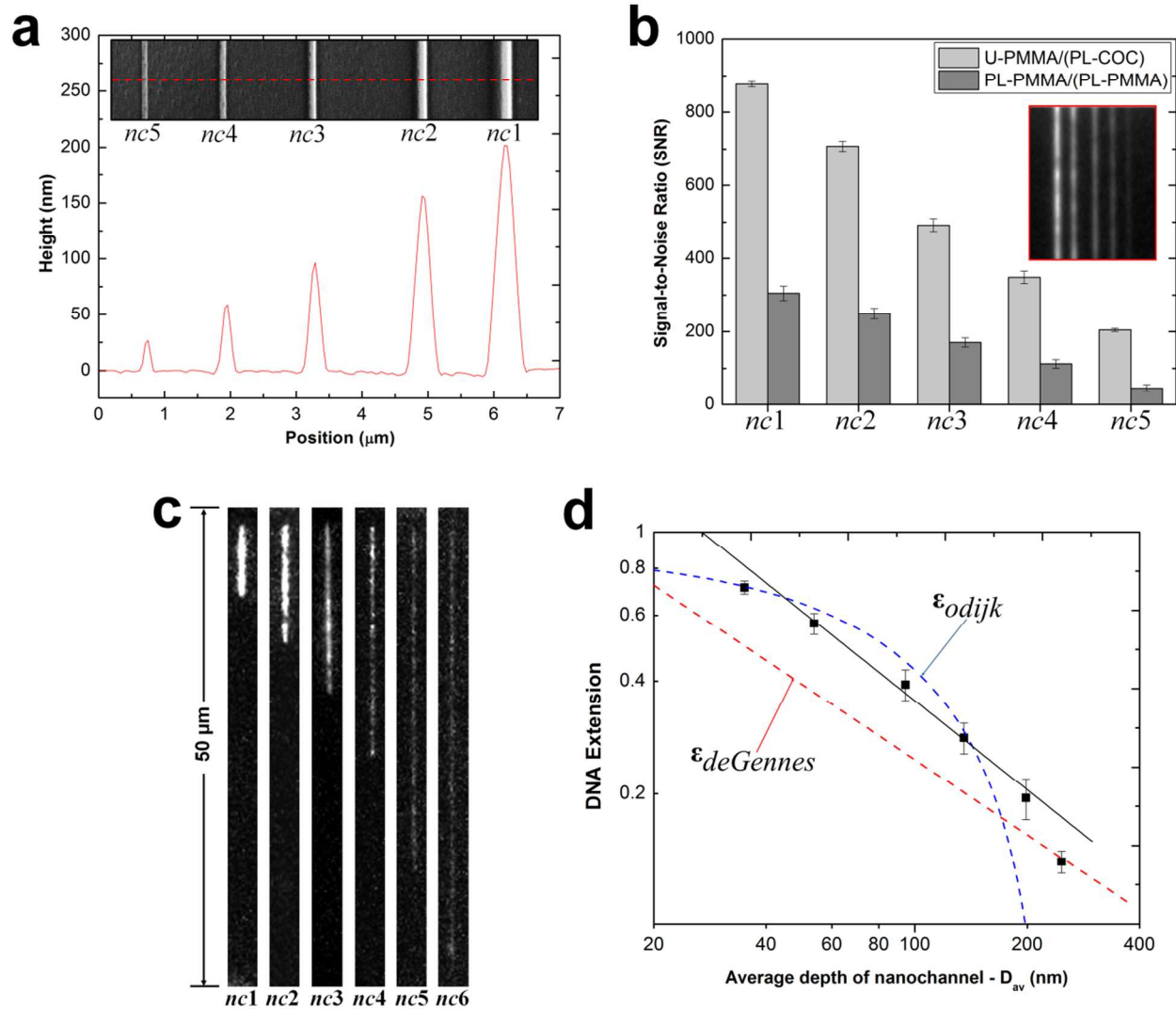


Figure 5. (a) AFM scan and SEM image (insert) of the UV curable resin stamp possessing a positive tone of the 2-D nanochannels. Channels were imprinted into PMMA with dimensions (width \times depth) of $nc1 = 300 \times 200$ nm, $nc2 = 250 \times 155$ nm, $nc3 = 190 \times 95$ nm, $nc4 = 150 \times 60$ nm and $nc5 = 110 \times 25$ nm. (b) Bar graphs showing the signal-to-noise ratio (SNR) at 2 s exposure time for the devices with untreated PMMA substrate enclosed with a plasma treated COC cover plate, U-PMMA/(PL-COC), and plasma treated substrate enclosed with a plasma treated PMMA cover plate, PL-PMMA/(PL-PMMA) filled with a 5 mM FITC solution. The error bars represent the standard deviation in measurements from ten separate devices. Insert shows unprocessed images of the seeding test for U-PMMA/(PL-COC). (c) Unprocessed representative frames of T4 DNA molecules elongated in enclosed nanochannels for the hybrid devices. Images were acquired at 10 ms exposure time with the driving field turned-off. Note that $nc6 = 35 \times 35$ nm. (d) Log-log plot showing the T4 DNA extension as a function of the geometric average depth of the nanochannels. The DNA extension was normalized to a total contour length (L_c) of 64 μ m for the dye-labeled molecules. The red and blue dashed lines are the deGennes and Odijk predictions, respectively. The black solid line is the best power-law fit to the data points obtained from the nanochannels with an average geometric depth range of 53 nm to 200 nm.

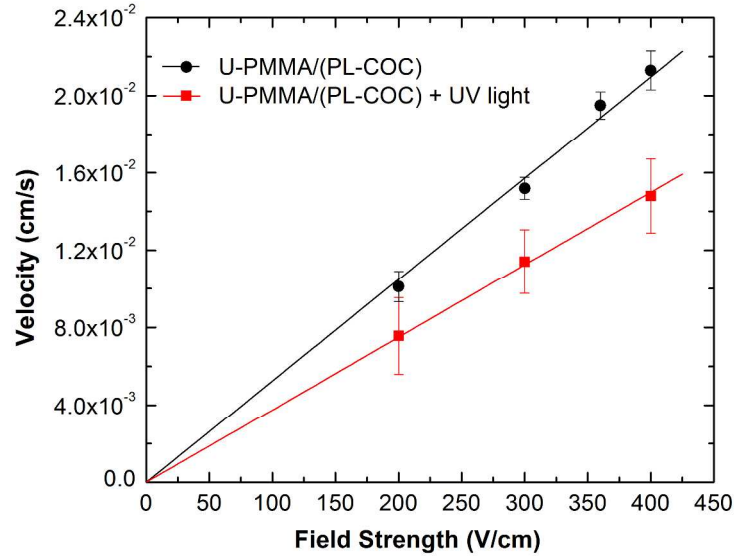


Figure 6. Graph showing the relationship between the translocation velocity (cm/s) and the field strength (V/cm) of λ -DNA translocating through hybrid devices before and after activation with UV/O₃ light. Each data point represents the mean of 20 events measured in 2 \times TBE buffer.